RSC Advances

PAPER

View Article Online
View Journal | View Issue

Cite this: *RSC Adv.*, 2025, **15**, 8663

Facile fabrication of robust superhydrophobic tapered needles for collection and transportation of underwater bubbles

Huicong Liu, [a] Huaxia Wang, [a] Liqun Zhu,[a] Weiping Li, [a] Haining Chen [a] and Weitao Liang *[b]

Received 27th September 2024
Accepted 19th February 2025

DOI: 10.1039/d4ra06971d

rsc.li/rsc-advances

The collection and transportation of underwater bubbles has attracted significant attention due to their wide range of applications in the mining, petroleum, and chemical industries. In this study, robust superhydrophobic tapered needles were successfully fabricated by spraying a superhydrophobic coating prepared by an organic–inorganic hybrid method. The prepared tapered needles present excellent surface stability and good superhydrophobicity with a contact angle (CA) of about 156°. The fabricated tapered needles demonstrate excellent performance in collection and transportation of underwater bubbles and the working mechanism was also thoroughly studied. The prepared robust superhydrophobic tapered needles provide a simple, efficient and economical way for collection and transportation of underwater bubbles.

1 Introduction

Micro-bubbles, characterized by their small diameter ranging from 10 to 50 μm, have garnered significant interest for their diverse applications,[1–3] including heavy medium coal preparation,[4] pipeline transportation,[5–9] drag reduction,[5,10–14] and more. In heavy-medium coal preparation, micro-bubbles alter the surface properties of target minerals, facilitating efficient fine coal separation. In pipeline transport, they increase the mass transfer area, effectively mitigating clogging issues. Additionally, when applied to the underwater surfaces of ships, micro-bubbles reduce skin friction between the hull and water, leading to a significant decrease in hydrodynamic resistance. On the other hand, micro-bubbles may also be harmful. For example, bubbles in crude oil will seriously affect the measurement accuracy of crude oil storage and transportation, resulting in reduced transportation and separation efficiency.[15–17] At the same time, micro-bubbles in crude oil also tend to absorb small solid impurities, which can cause blockages in pipelines and damage the transport and separation equipment. The presence of micro-bubbles in a water-based coating will produce micro pores, causing cavitation erosion and seriously affecting the protective effect of coatings.[15,18] Above all, it is meaningful to explore effective methods for collection and transportation of underwater bubbles. Traditional methods are mainly divided into physical methods and chemical methods,[19,20] such as the defoaming method, mechanical method, heating method, ultrasonic method, and more. However, these methods are either energy-intensive or necessitate the installation of additional costly specialized equipment. Furthermore, they exhibit low efficiency, particularly when dealing with small-diameter micro-bubbles. Consequently, there is an urgent need to develop a cost-effective and highly efficient method for the collection and transportation of underwater bubbles.

In recent years, super-wetting surfaces have garnered significant attention from researchers due to their broad applicability and ease of fabrication. Surfaces with tailored super-wetting properties have been engineered for a variety of applications, including corrosion protection,[21,22] water vapor collection,[23] and droplet directional movement,[24,25] among others. Some researchers have begun to explore the potential of super-wetting surfaces as a solution for manipulating underwater bubbles.[26–33] Ma Rui *et al.* reported a superhydrophobic sponge, which achieves rapid collection and stable storage of underwater bubbles. However, the superhydrophobic sponge did not achieve efficient control over the dynamic behavior of underwater bubbles, such as their movement or size distribution. Pei *et al.* reported a Janus membrane with superhydrophobic and superhydrophilic surfaces on opposite sides. It shows excellent unidirectional bubble permeability, and the results prove its effectiveness in underwater bubble manipulation. Yin *et al.* reported a trapezoidal platform featuring a micro/nano – structure through femtosecond laser direct cutting. The surface of this gradient platform exhibits superhydrophobicity in the air. Notably, this platform can gather bubbles in water and achieve the directional transport of

[a]School of Materials Science and Engineering, Beihang University, No. 37 Xueyuan Road, Haidian District, Beijing 100191, China
[b]b, School of Aeronautic Science and Engineering, Beihang University, No. 37 Xueyuan Road, Haidian District, Beijing 100191, China. E-mail: lwt@buaa.edu.cn

bubbles without external forces. Cao *et al.* reported a superhydrophobic copper helix capable of achieving controlled, directional bubble transport in water. The bubble velocity can be adjusted based on the helix distance. Yu *et al.* reported a lubricant-infused slippery (LIS) surface with exceptional water repellency, enabling efficient manipulation of bubbles in aqueous environments. However, its poor surface strength and high consumption significantly limit applications.

Our group has been paying much attention to the preparation and application of super-wetting films for a long time.[34–36] Ye *et al.* prepared a superhydrophobic coating with excellent mechanical durability, self-cleaning performance, and corrosion resistance through a novel organic synthesis and organic–inorganic composite method. Liang *et al.* prepared a composite coating for wax prevention in crude oil transportation. Yang *et al.* used the hydrolysis and condensation of tetraethoxysilane (TEOS) to form a silica sol–gel film while achieving controllable film material wettability. The thiol synthesis method based on click reaction has become a research hotspot in recent years due to its advantages such as low oxygen resistance, commercially accessible raw materials, few side reactions, simple operating conditions, and no use of metal catalysts.[37–45]

In this study, a facile click reaction was utilized to fabricate robust superhydrophobic coatings on tapered copper needles. Organic–inorganic composite coatings were fabricated *via* thiol-ene click reaction, leveraging its rapid kinetics and robust bonding characteristics. The influence of the organic-to-inorganic ratio on hydrophobicity was investigated, revealing that a composition of 0.4 g resin and 0.2 g SiO_2 achieved a water contact angle of 156°, indicating superior hydrophobicity. The durability of coatings was assessed *via* cyclic abrasion tests. A water contact angle of 147° persisted after 20 friction cycles, confirming mechanical robustness. The superhydrophobic tapered copper needles demonstrated efficient underwater bubble manipulation, attributed to synergistic effects of hierarchical microstructures and surface chemistry. The superhydrophobic surface stabilizes an air plastron (Cassie–Baxter state) on the tapered copper needle submerged underwater, creating interfacial pathways for sustained directional transport of microbubbles. Due to the tapered shape, the needles will produce a gradient of Laplace pressure, which can derive a directional driving force and transport droplets directionally.[46–48] The collection and transportation of bubbles by superhydrophobic copper needles under reverse gravity was also studied. This method will provide a simple and effective method to collect and transport micro-bubbles.

2 Materials and methods

2.1 Materials

All reagents were obtained at the highest purity available and used without further purification unless otherwise specified. Pentaerythritol tetra-3-mercaptopropionate (PETMP, Shanghai Aladdin Biochemical Technology Co., Ltd), benzoin dimethyl ether (Adamas Reagent Co., Ltd), acetone (Beijing Chemical Plant), dodecafluoroheptyl methacrylate, 3-(trimethoxysilyl) propyl methacrylate (Adamas Reagent Co., Ltd), tetraethoxysilane (TEOS, Guangzhou Xilong Chemical Co., Ltd), dibutyltin silicate (Tianjin Jinke Fine Chemical Research Institute), hydrophobic SiO_2 nanoparticles (7–40 nm, Shanghai Aladdin Biochemical Technology Co., Ltd), $CuSO_4$ (West long chemical).

2.2 Preparation of organic–inorganic composite coating

According to the free radical mechanism, the synthesize process mainly includes the following steps. At first, a certain amount of PETMP, benzoin dimethyl ether and acetone were added to the bottle in N2 atmosphere and synthesized at 25 °C ± 2 °C. After stirring uniformly, dodecafluoroheptyl methacrylate was slowly added into the bottle through a constant pressure dropping funnel and reacted under UV light for 1 h. When completed, 3-(trimethoxysilyl)propyl methacrylate was also slowly added into the bottle and reacted under UV light for 1 h. (PETMP : dodecafluoroheptyl methacrylate : 3-(trimethoxysilyl)propyl methacrylate = 1 : 2 : 2). After the reaction was completed, a light-yellow liquid of fluorosilicone resin is obtained. The above fluorosilicone resin was added to the solution containing hydrophobic nano-silica, and ethyl orthosilicate, dibutyltin dilaurate and acetone were added to obtain a dispersed and uniform mixed solution. Finally, the superhydrophobic coating of organic–inorganic composite was obtained by spraying the prepared solution on the glass sheet and placing it at room temperature 25 °C for 24 h or heating it to 80 °C for 0.5 h.

2.3 Preparation of tapered needles

A uniform-diameter copper wire (0.4 mm diameter, 8 cm length) underwent sequential ultrasonic cleaning in 1.0 mol L^{-1} hydrochloric acid, acetone, and ethanol, each for 5 minutes. Following deionized water rinsing, the wire was nitrogen-dried to complete pretreatment. The prepared wire was vertically mounted in an electrolytic cell (11 cm × 6 cm × 7 cm) using a copper–graphite electrode. The electrolyte consisted of $CuSO_4$ in 0.2 mol L^{-1} H_2SO_4 solution. During electrodeposition, continuous electrolyte circulation was maintained through a syringe pump system extracting solution at 0.5 mL s^{-1} for 10 extraction cycles. This dynamic flow regime facilitated the formation of a tapered copper needle structure. Post-processing included surface cleaning and nitrogen-protected ambient drying. For subsequent coating application, the tapered needle was vertically fixed on a rotation stage programmed for controlled clockwise rotation. A spray gun maintained at 30 kPa pressure was positioned 20 cm from the rotating substrate to ensure uniform deposition.

2.4 Characterization

The surface morphology of the fabricated coatings was characterized using field emission scanning electron microscopy (FESEM, JSM-7500F, JEOL, Japan). Chemical composition analysis was performed through Fourier transform infrared spectroscopy (FT-IR) recorded on a NEXUS-470 spectrometer (Nicolet, USA) employing the KBr-pellet method, with spectral acquisition ranging from 4000 to 500 cm^{-1} at 8 cm^{-1} resolution. Surface topography evaluation was conducted *via* atomic force microscopy (AFM, Veeco DI) in tapping mode under ambient conditions, utilizing a scan rate of 256 Hz over a 5 μm × 5 μm imaging

area. Wettability characteristics were determined using a KRÜSS DSA20 optical contact angle analyzer (Germany) *via* the sessile-drop method at ambient temperature. Static contact angles were measured with 5 μL droplets, while sliding angles were determined by incrementally tilting the stage until 10 μL droplets initiated movement. Mechanical durability assessments included knife-scratch resistance and sandpaper abrasion tests, following established protocols from previous studies. For standardized testing, coatings were deposited on glass substrates. The scratch resistance evaluation involved creating grid patterns on coated surfaces using a standardized cutting tool. Abrasion resistance was quantified by subjecting specimens (100 g loading) to linear abrasion against 800-grit sandpaper (0.5 kPa pressure) along orthogonal directions. Each test cycle consisted of a 10 cm linear abrasion followed by 90° specimen rotation. Post-abrasion hydrophobicity was monitored through sequential contact angle measurements after predetermined test cycles.

3 Results and discussion

3.1 Reaction mechanism and surface morphology analysis of prepared organic–inorganic composite coating

The thiol-ene click reaction mechanism and its kinetic behavior have garnered significant attention from the global materials science community since their discovery. This surface modification strategy enables simultaneous introduction of functional groups and enhancement of critical material properties including adhesion and hydrophobicity. As illustrated in Fig. 1(a), the reaction mechanism bifurcates based on olefin configuration types. The thiol-alkene system operates through a radical chain-transfer mechanism, where thiyl radicals (–S·) initiate nucleophilic attack on the carbon–carbon double bond (C=C), subsequently propagating the active site through chain transfer processes. The radical-mediated thiol-ene addition proceeds through iterative chain propagation, while thiol-methacrylate systems with conjugated olefins follow a Michael addition pathway. In the latter mechanism, the nucleophilic thiolate anion (S^-) attacks the β-carbon of the electron-deficient C=C bond, forming a carbanion intermediate that regenerates active species *via* proton abstraction from either –SH groups or alkali cations. This chain-propagation mechanism significantly enhances reaction kinetics. Subsequent integration of –$Si(OCH_3)_3$ low-surface-energy groups into the resin matrix, coupled with TEOS as a curing agent and dibutyltin dilaurate catalysis, promotes siloxane (Si–O–Si) network formation through hydrolytic condensation. As illustrated in Fig. 1(b), this cross-linked architecture synergistically optimizes both hydrophobicity and mechanical strength in the final coating.

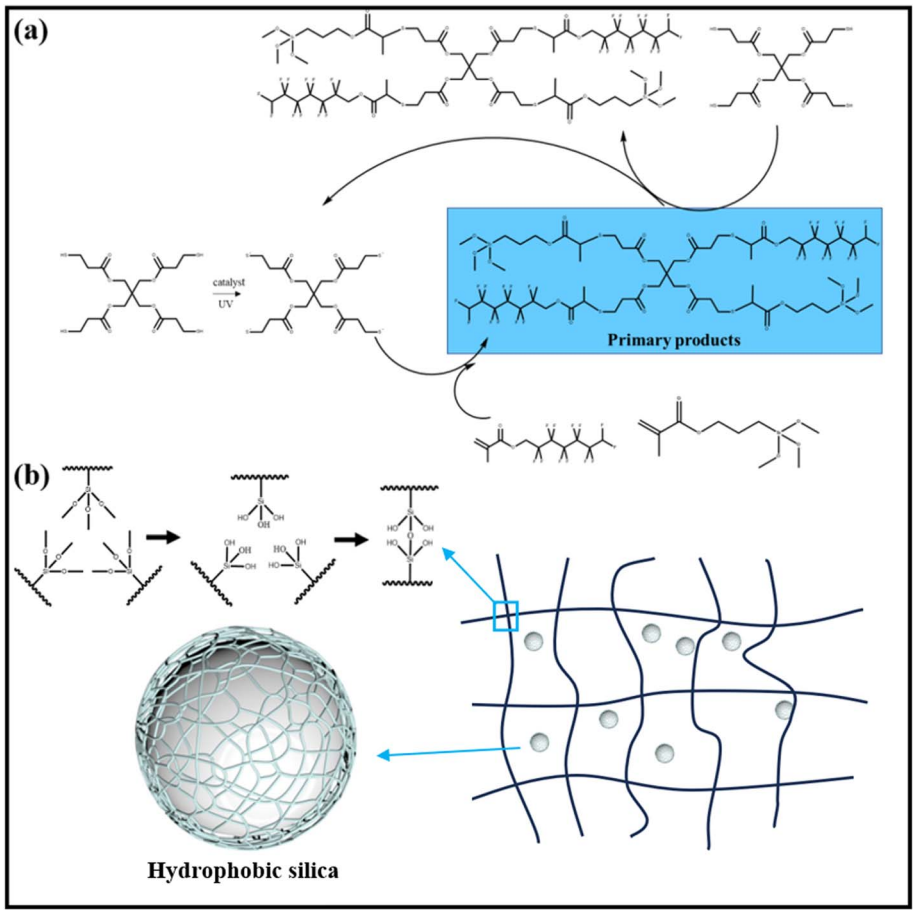

Fig. 1 Schematic diagram of organic–inorganic composite coating preparation. (a) Thiol-ene click chemistry reaction based on free radical mechanism; (b) schematic diagram of silane hydrolysis to form a network structure.

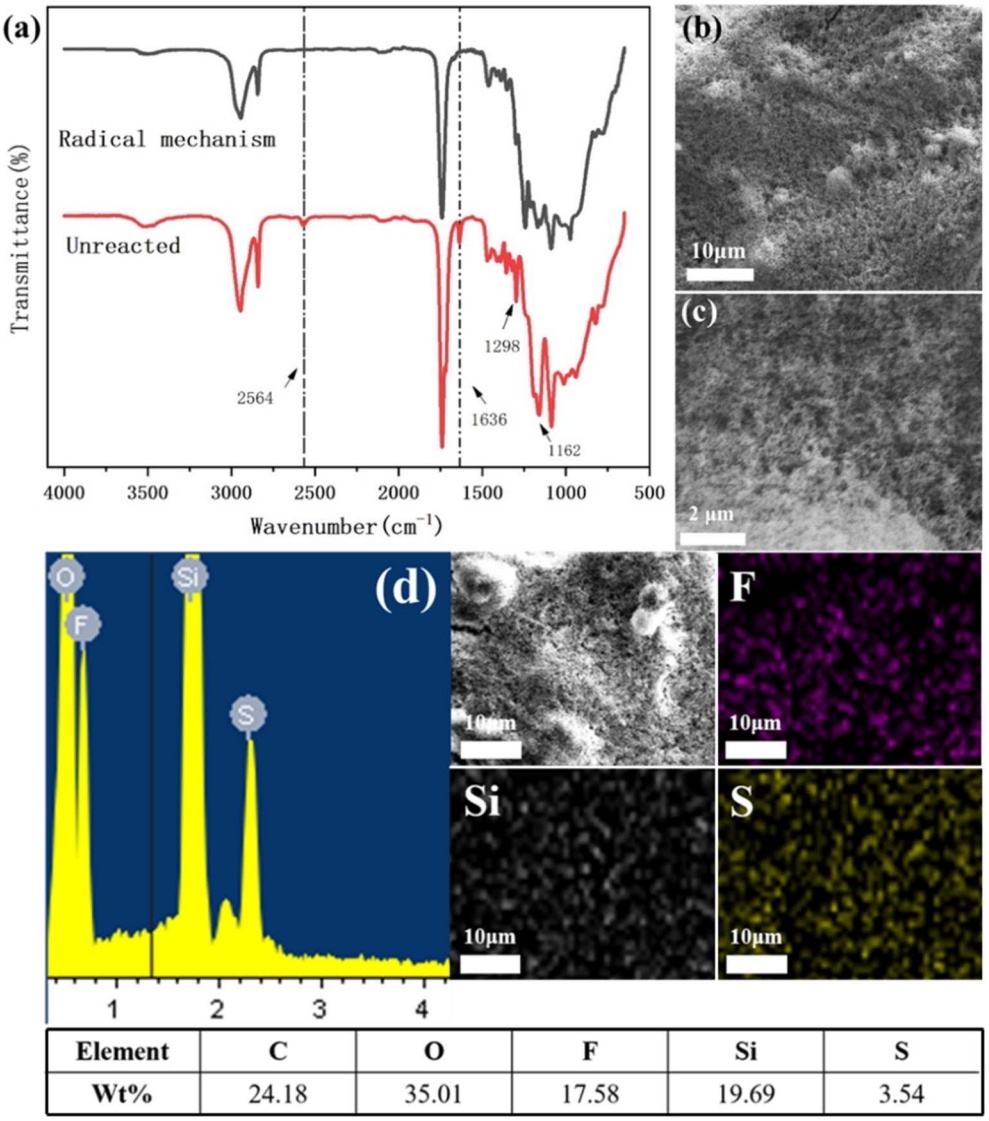

Element	C	O	F	Si	S
Wt%	24.18	35.01	17.58	19.69	3.54

Fig. 2 (a) FT-IR images of FCS-SiO_2 particles before and after modification; SEM micrographs of modified SiO_2 particles at (b) low and (c) high magnification; (d) EDS spectrums of modified SiO_2 particles and corresponding element distribution images of F, S and Si.

Fig. 2 characterizes the surface morphology and chemical composition of modified SiO_2 particles prepared *via* a photo-initiated fluorosilicone resin synthesis. FT-IR analysis in Fig. 2(a) reveals significant spectral changes post-modification: the broadened and attenuated –OH stretching vibration at 3433 cm^{-1} confirms successful silanol group consumption through chemical grafting. Characteristic perfluoroalkyl absorptions at 1204 cm^{-1} and 1149 cm^{-1}, combined with the absence of residual C=C (1636 cm^{-1}) and –SH (2564 cm^{-1}) signals, demonstrate complete thiol-ene conversion and successful integration of fluorinated moieties into the resin matrix. SEM imaging at multiple magnifications in Fig. 2(b and c) reveals inherent micro/nanoscale hierarchical structures formed during spray deposition. High-resolution imaging confirms the coexistence of micron-sized aggregates and nanoscale surface asperities from fumed SiO_2, collectively establishing a porous multilevel morphology. EDS elemental mapping in Fig. 2(d) verifies uniform surface distribution of F (17.58 ± 0.13 wt%), S, and Si – with fluorine enrichment (*vs.* bulk 11%) indicating surface-segregation of low-surface-energy fluoropolymer chains. The detected sulfur and silicon derive respectively from PETMP crosslinkers and SiO_2 nanoparticles, consistent with the designed formulation.

3.2 Influence of surface composition on hydrophobicity

Coatings featuring micro-nano-scale roughness structures often exhibit mechanical fragility and susceptibility to abrasion, particularly on rigid substrates. Organic–inorganic nanocomposites have emerged as a promising strategy to address this limitation, achieved either through polymer-grafted nanoparticles or dispersion of surface-modified nanoparticles within polymeric matrices. Crucially, the organic/inorganic mass ratio critically determines the hydrophobic performance during composite fabrication, necessitating systematic optimization. Table 1 shows 9 formulations for follow-up research.

Table 1 Hydrophobic coatings of different fluorosilicone and silica resins

Group	Fluor silicone/g	SiO_2/g	Acetone/g
A	0.0	0.2	5.0
A	0.2	0.2	5.0
A	0.4	0.2	5.0
A	0.6	0.2	5.0
B	0.4	0.0	5.0
B	0.4	0.05	5.0
B	0.4	0.1	5.0
B	0.4	0.2	5.0
B	0.4	0.4	5.0

During the preparation process, the ratio of SiO_2 particles to resin plays a great role in the hydrophobic effect. In order to determine the most suitable ratio, two sets of samples were prepared: the SiO_2 particles of group A were fixed at 0.2 g, and the resin was 0 g, 0.2 g, 0.4 g, and 0.6 g. The resin of group B was fixed at 0.4 g, and the SiO_2 particles were 0 g, 0.05 g, 0.1 g, 0.2 g, and 0.4 g. The solvent of the two groups is 5 g of acetone, and the curing agent is 0.2 g.

3.2.1 Effect of fluorosilicone on hydrophobicity. The hydrophobicity of coatings is principally governed by two critical factors: low surface energy characteristics and hierarchical surface roughness. To systematically investigate the SiO_2/resin mass ratio's impact on water-repellent performance, FT-IR analysis was conducted on component B formulations in Fig. 3(c). Spectral analysis reveals characteristic C–F stretching vibrations within the 1298–1162 cm^{-1} range, demonstrating successful perfluoroalkyl group incorporation. Notably, the progressive intensification of these absorption bands with increasing resin content confirms enhanced surface fluorination – a critical determinant of surface energy reduction. Concurrently, emerging hydroxyl group signals near 3000 cm^{-1} suggest competing hydrophilic interactions, though their relative intensity remains subordinate to dominant hydrophobic functionalities. Optimal hydrophobicity was achieved at 0.4 g resin loading, evidenced by water contact angles exceeding 150° in Fig. 3(a and b). This performance maximum correlates with the synergistic balance between fluorocarbon coverage and surface roughness preservation.

3.2.2 Effect of SiO_2 on hydrophobic effect. In order to explore the influence of SiO_2 particles on wettability, the SEM was used to characterize the coatings of component B. The surface morphology of samples with different SiO_2 particle masses is shown in Fig. 4(a–d). When the mass of SiO_2 particles is 0.05 g, the coating surface is relatively smooth. The irregular pattern in the figure is fluorosilicone resin, and the SiO_2 particles do not provide enough roughness, Fig. 3(b) shows its water contact angle is only 73.5°, which fails to meet the requirement of hydrophobic; when the mass of SiO_2 particles is 0.1 g, the roughness of the coating increases significantly, but there are

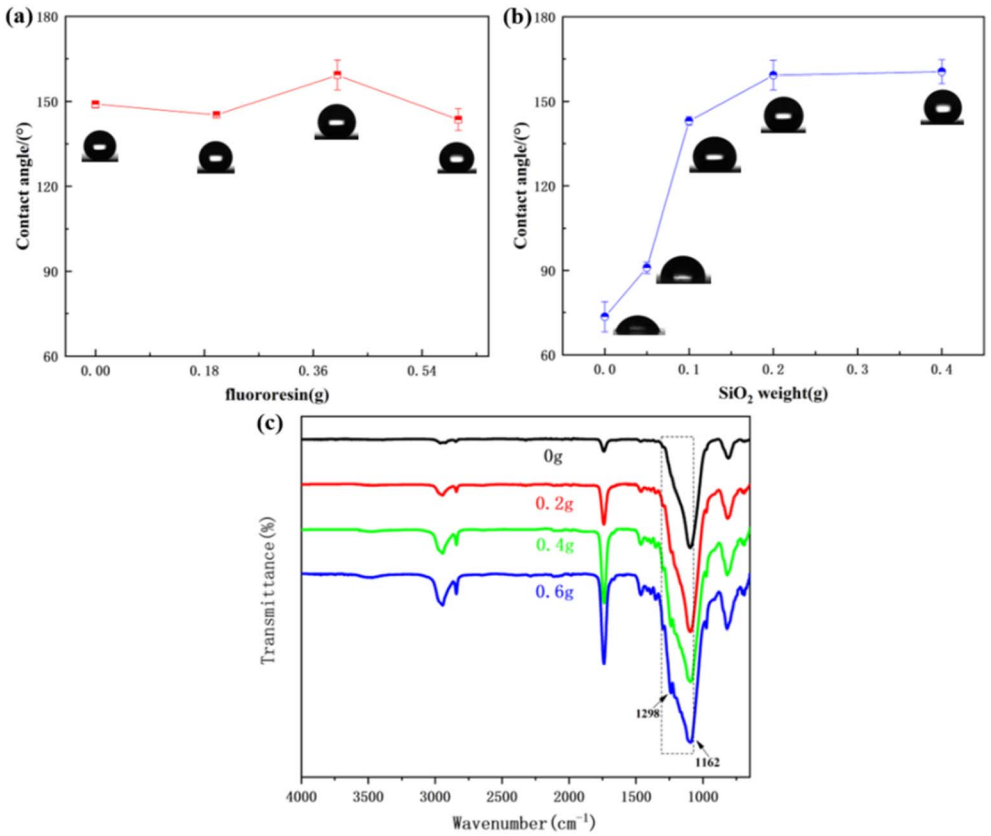

Fig. 3 (a) WCAs with different resin content. (b) Hydrophobic angles of samples with different SiO_2 particle masses. (c) Infrared spectra of different resin contents.

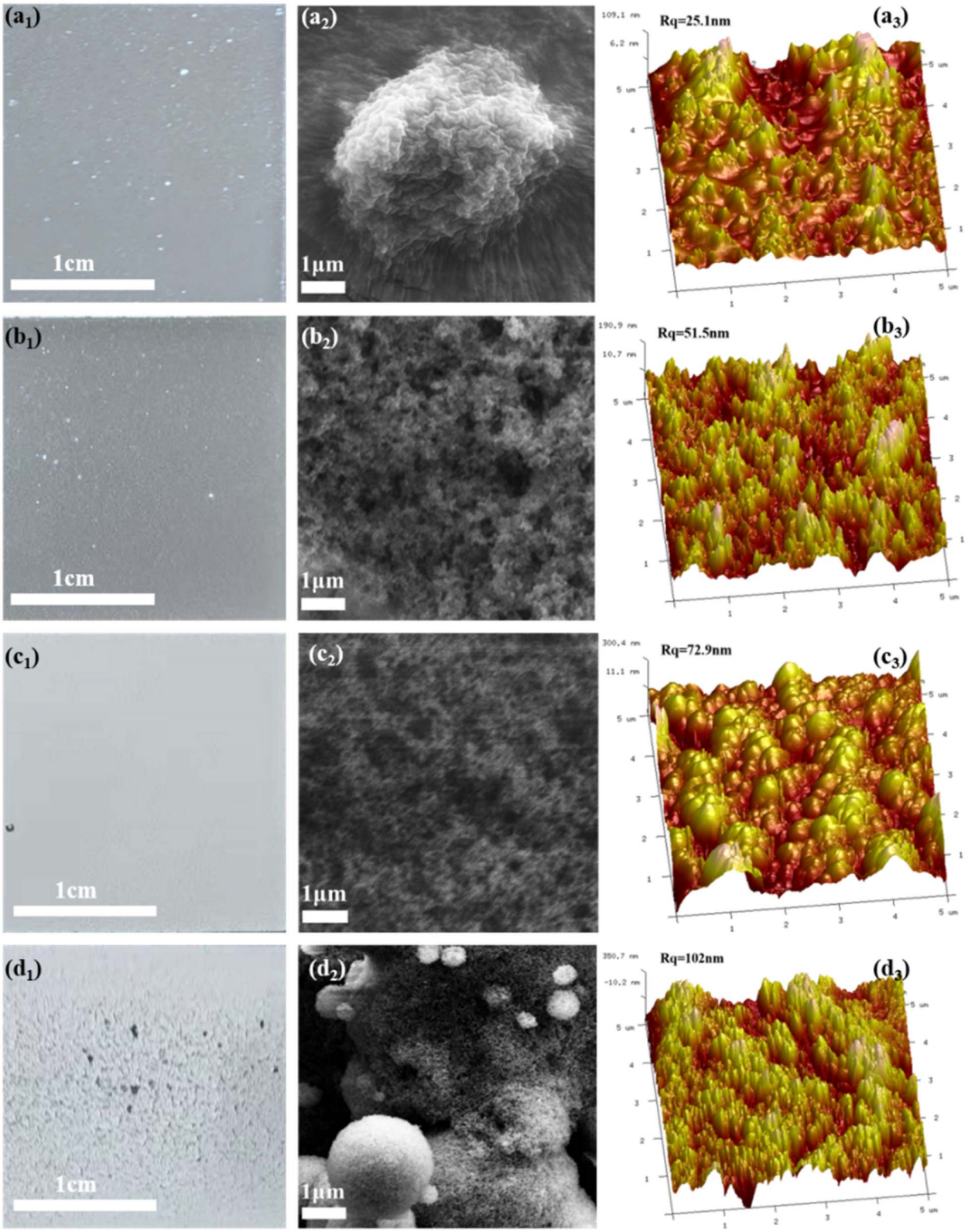

Fig. 4 The surface macro morphology, micro morphology and roughness of samples with different SiO_2 particle quality (a) 0.05 g (b) 0.1 g (c) 0.2 g (d) 0.4 g.

obvious cavities on the surface, and the distribution of SiO_2 particles is uneven, its hydrophobic angle is slightly increased to 90.9°, barely meeting the requirement of hydrophobic; when the mass of SiO_2 particles is 0.4 g in Fig. 4(d), even though the hydrophobic angle is 160°, but it will be caused by too many SiO_2 particles, which can cause multi-initiated reunion and

poor film formation. Therefore, the effect is best when the mass of SiO_2 particles is 0.2 g. It can be seen from the Fig. 4(c_1) shows that the SiO_2 particles are evenly distributed, with less agglomeration and voids, and provide sufficient roughness to the coating surface, and the hydrophobic coating will be more hydrophobic and the effect is best, its water contact angle is 159.3°, which meets the requirement of superhydrophobic.

3.3 The superhydrophobic property of the prepared coating

The fluorosilicone resin–SiO_2 superhydrophobic composite coating exhibits excellent superhydrophobicity, with a static water contact angle of up to 156° on the glass substrate. To evaluate its self-cleaning potential, dynamic tests were conducted. As shown in Fig. 5(a), a 10 μL water droplet rapidly slides off the inclined surface (tilt angle: 3°) within 273 ms, indicating the coating's low adhesion properties, which facilitate bubble transportation. Fig. 5(b) further characterizes the dynamic adhesion behavior: when a 5 μL water droplet on a needle contacts the coating surface, a defined pressure is applied to deform the droplet. Subsequently, the droplet detaches without leaving any residue, confirming the coating's exceptional superhydrophobicity.

3.4 Collect transport bubbles

Numerous studies have demonstrated that a structurally modified conical surface generates gradients of Laplace pressure and surface free energy, creating a directional driving force for droplet collection and transport. Inspired by this mechanism, we aim to introduce analogous gradients onto conical surfaces to enable continuous collection and directional transport of microbubbles in aqueous media. In this work, a superhydrophobic coating was integrated onto copper needles to achieve efficient microbubble manipulation in deionized water. Upon immersion, the superhydrophobicity of the coated needle induces a stable air layer underwater, providing a low-resistance pathway for microbubble transportation. The Laplace pressure gradient arising from the conical geometry serves as the primary driving force, directing bubbles along the needle surface. This approach offers a simple yet effective strategy for microbubble elimination in liquid systems.

As shown in Fig. 6, on the surface of the horizontally placed superhydrophobic copper needle, there are four forces acting on the moving bubbles, namely Laplace pressure (F_L), synthetic resistance (F_R) generated by the liquid and lubricating layer, buoyancy (F_B), and the adhesion of the superhydrophobic copper needle surface to the air bubbles (F_A). F_L is the driving force for the directional movement of bubbles induced by the cone shape of a superhydrophobic copper cone.[49–52]

$$F_L \approx 2l_1 l_2 \left(\frac{1}{R_1} - \frac{1}{R_2}\right) S \sin\alpha \quad (1)$$

where R_1 and R_2 are the local radii on opposite sides of the bubble, S is the area of the area surrounded by the bubble, and α is the half-vertex angle of the cone. Since the bubble is attached to the surface of the superhydrophobic copper cone, there will be a difference in radius between the two opposite sides of the bubble. Therefore, the F_L directionally drives the bubbles on the surface of the superhydrophobic copper needle from its tip to its bottom. When air bubbles move on a smooth surface in an aqueous environment, the resistance generated by the liquid and the viscous layer must be considered. The resultant resistance (F_R) can be calculated as follows:[53–55]

$$F_R = \frac{1}{2} C_D \rho v^2 A + a v^k \quad (2)$$

where C_D and ρ are the resistance coefficient and the density of the aqueous medium, respectively; v is the transmission speed of the bubble; A is the cross-sectional area of the bubble; a and k are uncertain parameters derived from the resistance of the

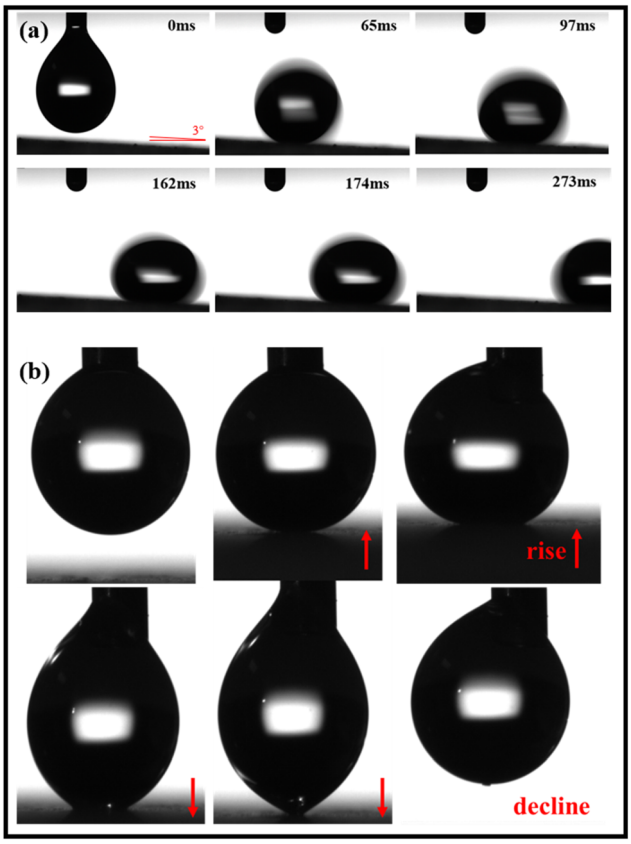

Fig. 5 Superhydrophobic properties (a) rolling angle (b) dynamic adhesion behavior.

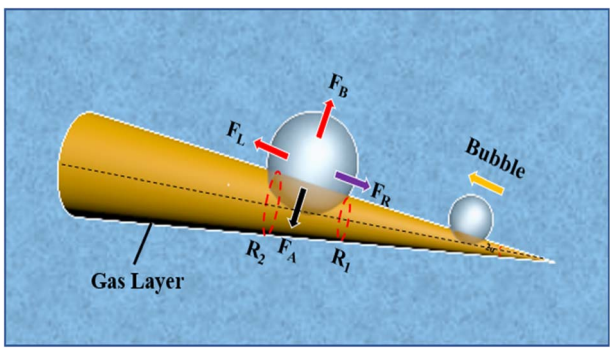

Fig. 6 Schematic diagram of Laplace driving force.

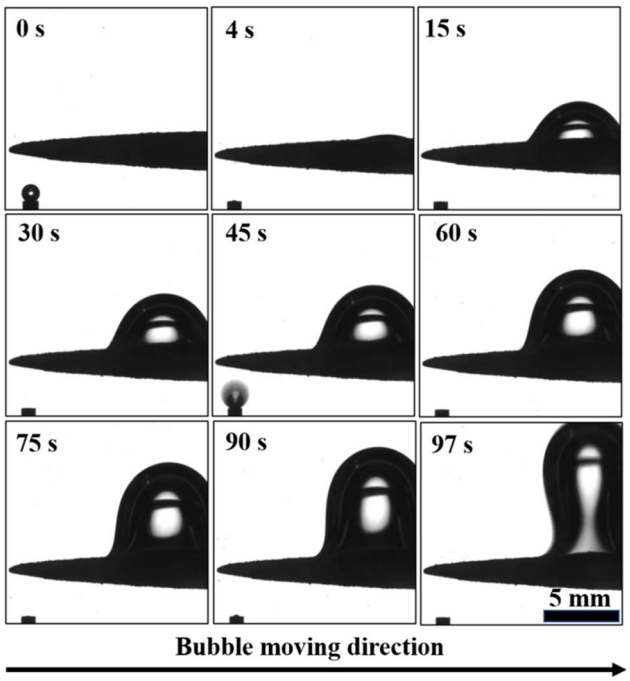

Fig. 7 Microbubble collection and transportation experiment.

lubricating layer. F_B is determined by the volume of the bubble (V), the density of the liquid (ρ), and the acceleration of gravity (g), and can be expressed as follows:

$$F_B = \rho g V \quad (3)$$

F_A can be derived as follows:[56,57]

$$F_A = \gamma_{l_1 l_2} L_{TCL} \sin\beta \quad (4)$$

where L is the length of the three-phase contact line and β is the effective contact angle of the bubble on the smooth surface. For the case where the bubble moves horizontally on the surface of the superhydrophobic copper cone, F_A can resist F_B, and its resultant force is equal to zero in the vertical direction.

The collection and transport processes of microbubbles in water by superhydrophobic copper needles were studied. To prevent carbonic acid interference from dissolved CO_2, a closed pipe flow system with a flow rate of 0.5 μL s^{-1} was utilized. The copper needle was positioned horizontally in deionized water to suppress buoyancy effects on bubble dynamics. As shown in Fig. 7, microbubbles contacting the needle surface spread rapidly, confirming its superaerophilic behavior in water. These bubbles migrated from the needle's tip to its tail at 20.5 ± 0.5 mm s^{-1}, merging into a single large bubble. At 97 s, buoyancy exceeded the adhesive force, causing detachment of the 48 μL bubble. This cycle repeated continuously, enabling sustained microbubble collection and transport. The superhydrophobic copper needle was taken out, stood at room temperature for 24 h, and then immersed in water again, it still had the ability to collect and transport bubbles. The application of superhydrophobic copper needles in crude oil exploitation can reduce the bubble content and improve the efficiency of crude oil exploitation; when applied to waterborne coatings, it can improve the film-forming property and make the coating more uniform.

Fig. 8 investigates bubble collection and transport by the superhydrophobic copper needle under reverse gravity conditions. At a tilt angle of 20°, the average transport velocity is 17.4 ± 0.5 mm s^{-1} with a transport distance of 0.6 cm. When the tilt angle increases to 90°, the velocity decreases to 6.5 ± 0.5 mm s^{-1} and the distance shortens to 0.5 cm. These results confirm that the needle can collect and transport bubbles against gravity. Comparing these data with the 0° tilt angle case (horizontal placement, Fig. 7), we observe a clear trend: as the tilt angle increases, buoyancy increasingly opposes the adhesive force, leading to slower transport speeds and shorter distances. Nevertheless, the needle maintains functionality even at 90°,

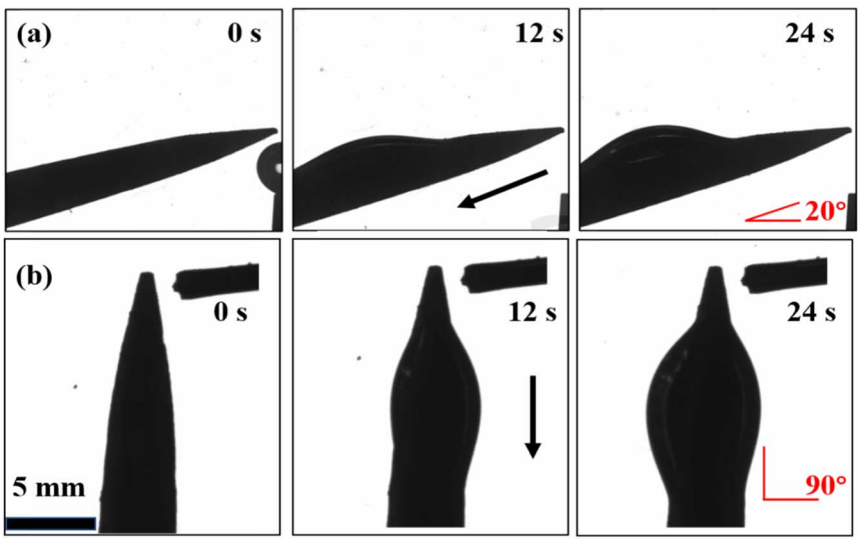

Fig. 8 Superhydrophobic copper needles collect and transport air bubbles against gravity. (a) 20° (b) 90°.

demonstrating its robustness in overcoming gravitational effects.

3.5 Stability

The limited mechanical durability of superhydrophobic surfaces poses a significant challenge for their real-world applications. To address this, we systematically evaluated the robustness of an organic–inorganic composite coating through standardized sandpaper abrasion tests and knife scratch experiments.[58,59] As illustrated in Fig. 9(a), the abrasion protocol involved cyclically moving the coating (under a 100 g load) across 800# SiC sandpaper—10 cm laterally, followed by a 90° rotation and another 10 cm longitudinal movement—to simulate severe mechanical wear. Remarkably, after 20 such cycles, the coating retained a water contact angle of 147° in Fig. 9(b), indicating robust mechanical resistance. This durability stems from the coating's "bulk superhydrophobicity", a structural design where hydrophobic SiO_2 nanoparticles and interconnected cavities are distributed not only on the surface but also throughout the interior. Consequently, even if the top layer is abraded, the underlying hydrophobic network maintains non-wettability. Comparative analysis with the DMS/ODA-PDA@PI nanofibrous membrane reported by Wenjing Ma *et al.*,[58] revealed that our coating achieved a higher post-abrasion water contact angle (147° *vs.* 135° after 20 cycles), underscoring its superior mechanical resilience. Furthermore, the coating's ability to repel impacting droplets—causing them to retract or rebound—significantly reduces ice nucleation sites, suggesting strong potential for anti-icing applications in harsh environments. These results collectively demonstrate that the synergy of structural design and material composition can effectively mitigate the mechanical fragility of superhydrophobic coatings.

As shown in Fig. 9(c), in the blade scratch test,[60] after the blade is scratched according to the preset route, the coating still maintains superhydrophobic properties. After the test, when the dyed water droplets were dropped onto the surface of the scribed coating, they rolled off quickly without any adhesion, indicating the excellent anti-scratch stability of the composite coating.

In the actual application process, the coating may come into contact with robust acid or alkaline substances. In order to evaluate the chemical stability of the composite coating in an acid-base environment, this section adopts two methods, using aqueous solutions of different pH values to test the static contact angle of the coating surface and immersing the coating in aqueous solutions of different pH values. After a certain period of time, take out the coating and measure the static contact angle for evaluation. Fig. 9(d) shows the static contact angles of aqueous solutions with different pH values on the coating surface. It can be seen from the figure that solutions with different acidity and alkalinity all exhibit excellent

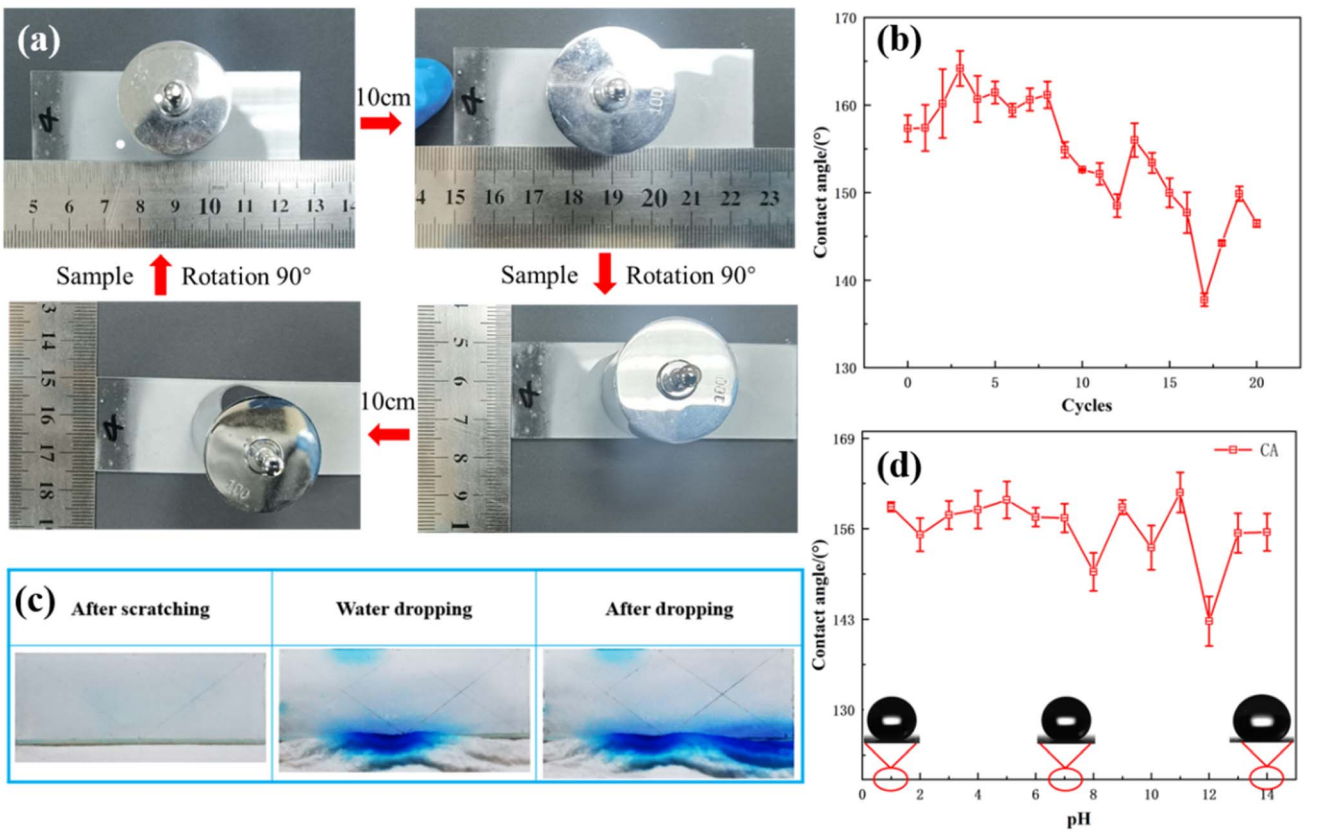

Fig. 9 (a) Wear diagram (b) the relationship between the number of sandpaper abrasion test cycles and the wettability of the coating surface (c) scratch test (d) the static contact angle of water droplets with different pH values on the surface of the composite coating.

superhydrophobicity on the surface of the composite coating. The contact angle of acidic droplets is generally higher and more stable than that of alkaline droplets. By comparing with the DMS/ODA-PDA@PI nanofibrous membrane prepared by Wenjing Ma *et al.*,[58] the performance of this coating is better in acidic environment, and the hydrophobic angle is more than 154°. However, in alkaline environment, it is slightly insufficient and fluctuates greatly. This may be due to the high affinity of the nanoparticles on the surface of the coating with the sodium hydroxide solution, which allows the alkaline aqueous solution to diffuse into the porous micro–nano structure with air hidden on the surface of the coating. Further, the composite coating is immersed in a solution of hydrochloric acid and sodium hydroxide with pH of 1 and 14. The experimental results show that after immersing in a hydrochloric acid solution with a pH of 1 for 10 hours, there is no change on the surface of the coating, and the surface remains dry. After removal from the solution, the surface of the coating remains dry and does not stick to the solution. These results indicate that the superhydrophobic composite coating has outstanding stability in a robust acid environment. However, for a robust alkaline sodium hydroxide solution with a pH of 14, the surface of the coating was partially wetted and lost its mirror effect after 1 hour of soaking. After soaking for 10 hours, the surface of the composite coating was completely wetted. This indicates that the composite coating has poor resistance to robust alkaline environments.

4 Conclusions

In this article, a fast and simple method for preparing superhydrophobic coating by spraying perfluoro thiol/acrylate resin containing hydrophilic silica nanoparticles was introduced. The hydrophobic angle reaches 156°, and it has excellent mechanical properties and acid resistance. The spray deposition method of the nanoparticle-loaded resin provides the coating with a layered rough morphology on a wide range of substrates. Combined with copper cones, it can be used for gas collection and transportation in gas–water–solid three-phase systems. The superhydrophobic copper cone continuously collects microbubbles from the carbonated water, and then directionally transport them to the bottom surface driven by the gradient of Laplace pressure and surface free energy. The transport direction of the microbubbles can be controlled by the superhydrophobic copper cone.

Data availability

The data supporting this study are available on request from the corresponding author.

Conflicts of interest

The authors declare that they have no known competing financial interests or personal relationships that could have appeared to influence the work reported in this paper.

Acknowledgements

The authors are very grateful to the support from National Key Research and Development Program (2023YFB3408200).

References

1 P. Khan, W. Zhu, F. Huang, W. Gao and N. A. Khan, Micro–nanobubble technology and water-related application, *Water Supply*, 2020, **20**, 2021–2035.
2 T. Temesgen, T. T. Bui, M. Han, T.-I. Kim and H. Park, Micro and nanobubble technologies as a new horizon for water-treatment techniques: a review, *Adv. Colloid Interface Sci.*, 2017, **246**, 40–51.
3 A. Agarwal, W. J. Ng and Y. Liu, Principle and applications of microbubble and nanobubble technology for water treatment, *Chemosphere*, 2011, **84**, 1175–1180.
4 L. Dong, Y. Zhao, L. Peng, J. Zhao, Z. Luo, Q. Liu and C. Duan, Characteristics of pressure fluctuations and fine coal preparation in gas-vibro fluidized bed, *Particuology*, 2015, **21**, 146–153.
5 J. H. Moon, D. Fadda, D. H. Shin, J. S. Kim, J. Lee and S. M. You, Boiling-driven, wickless, and orientation-independent thermal ground plane, *Int. J. Heat Mass Transfer*, 2021, **167**, 120817.
6 G. E. O. Celis, C. M. P. Rosero, J. B. R. Loureiro and A. P. Silva Freire, Breakup and coalescence of large and small bubbles in sudden expansions and contractions in vertical pipes, *Int. J. Multiphase Flow*, 2021, **137**, 103548.
7 H. Setoodeh, W. Ding, D. Lucas and U. Hampel, Modelling and simulation of flow boiling with an Eulerian-Eulerian approach and integrated models for bubble dynamics and temperature-dependent heat partitioning, *Int. J. Therm. Sci.*, 2021, **161**, 106709.
8 Z.-K. Gao, M.-X. Liu, W.-D. Dang, C. Ma, L.-H. Hou and X.-L. Hong, Multilayer limited penetrable visibility graph for characterizing the gas-liquid flow behavior, *Chem. Eng. J.*, 2021, **407**, 127229.
9 J. Cheng, S. Liu, W. Guo, Y. Song, S. Kumar, A. A. Kubar, Y. Su and Y. Li, Developing staggered woven mesh aerator with three variable-micropore layers in recycling water pipeline to enhance CO_2 conversion for improving Arthrospira growth, *Sci. Total Environ.*, 2021, **760**, 143941.
10 L. Musango, S. John and M. Lloyd, CFD-DEM simulation of Small-Scale Challenge Problem 1 with EMMS bubble-based structure-dependent drag coefficient, *Particuology*, 2021, **55**, 48–61.
11 D. Gurera and B. Bhushan, Bioinspired movement of gas bubbles: composition, applications, generation, contact angle, and movement – an overview, *Mol. Syst. Des. Eng.*, 2020, **5**, 1555–1577.
12 F. Picella, J. C. Robinet and S. Cherubini, On the influence of the modelling of superhydrophobic surfaces on laminar–turbulent transition, *J. Fluid Mech.*, 2020, **901**, A15.
13 Y. Gao, M. Wu, Y. Lin and J. Xu, Trapping and control of bubbles in various microfluidic applications, *Lab Chip*, 2020, **20**, 4512–4527.

14 L. Jiao and J. M. Floryan, Use of transpiration for reduction of resistance to relative movement of parallel plates, *Phys. Rev. Fluid.*, 2021, **6**, 014101.
15 Z. Liu, X. Gao, L. Du, J. Li, Y. Kuang and B. Wu, Corrosion behavior of low-alloy steel with martensite/ferrite microstructure at vapor-saturated CO_2 and CO_2-saturated brine conditions, *Appl. Surf. Sci.*, 2015, **351**, 610–623.
16 E. Aljallis, M. A. Sarshar, R. Datla, V. Sikka, A. Jones and C.-H. Choi, Experimental study of skin friction drag reduction on superhydrophobic flat plates in high Reynolds number boundary layer flow, *Phys. Fluids*, 2013, **25**, 025103.
17 D. A. López, T. Pérez and S. N. Simison, The influence of microstructure and chemical composition of carbon and low alloy steels in CO_2 corrosion. A state-of-the-art appraisal, *Mater. Des.*, 2003, **24**, 561–575.
18 S. S. Kolesov, I. Kostitsyna, A. Shakhmatov, A. Davydov, R. V. Kizitov, A. B. Laptev, V. A. Polyansky, I. A. Golubev, A. A. Markov, A. Groysman, S. Webster, A. V. Shakhmatov, A. A. Alkhimenko, R. Badrak, V. V. Burlov, S. Y. Mushnikova, O. V. Shvetsov, M. Klapper, A. Dam, B. Ghai and Y. I. Kuznetsov, Study of corrosion behavior of carbon and low-alloy steels in CO_2-containing environments, *E3S Web Conf.*, 2019, **121**, 04006.
19 P. G. Kougias, P. Tsapekos, K. Boe and I. Angelidaki, Antifoaming effect of chemical compounds in manure biogas reactors, *Water Res.*, 2013, **47**, 6280–6288.
20 P. G. Kougias, K. Boe, P. Tsapekos and I. Angelidaki, Foam suppression in overloaded manure-based biogas reactors using antifoaming agents, *Bioresour. Technol.*, 2014, **153**, 198–205.
21 S. Wang, Y. Wang, Y. Zou, G. Chen, J. Ouyang, D. Jia and Y. Zhou, Biologically Inspired Scalable-Manufactured Dual-layer Coating with a Hierarchical Micropattern for Highly Efficient Passive Radiative Cooling and Robust Superhydrophobicity, *ACS Appl. Mater. Interfaces*, 2021, **13**, 21888–21897.
22 R. Jain and R. Pitchumani, Facile Fabrication of Durable Copper-Based Superhydrophobic Surfaces *via* Electrodeposition, *Langmuir*, 2017, **34**, 3159–3169.
23 V. Sharma, H. Ali-Löytty, A. Koivikko, K. Yiannacou, K. Lahtonen and V. Sariola, Copper Oxide Microtufts on Natural Fractals for Efficient Water Harvesting, *Langmuir*, 2021, **37**, 3370–3381.
24 M. R. Hassan, J. Zhang and C. Wang, Digital Microfluidics: Magnetic Transportation and Coalescence of Sessile Droplets on Hydrophobic Surfaces, *Langmuir*, 2021, **37**, 5823–5837.
25 Y. Si and Z. Dong, Bioinspired Smart Liquid Directional Transport Control, *Langmuir*, 2020, **36**, 667–681.
26 B. Chen, T. Wada and H. Yabu, Underwater Bubble and Oil Repellency of Biomimetic Pincushion and Plastron-Like Honeycomb Films, *Langmuir*, 2020, **36**, 6365–6369.
27 L. Xie, C. Shi, X. Cui and H. Zeng, Surface Forces and Interaction Mechanisms of Emulsion Drops and Gas Bubbles in Complex Fluids, *Langmuir*, 2017, **33**, 3911–3925.
28 R. Ma, J. Wang, Z. Yang, M. Liu, J. Zhang and L. Jiang, Bioinspired Gas Bubble Spontaneous and Directional Transportation Effects in an Aqueous Medium, *Adv. Mater.*, 2015, **27**, 2384–2389.
29 C. Pei, Y. Peng, Y. Zhang, D. Tian, K. Liu and L. Jiang, An Integrated Janus Mesh: Underwater Bubble Antibuoyancy Unidirectional Penetration, *ACS Nano*, 2018, **12**, 5489–5494.
30 K. Yin, S. Yang, X. Dong, D. Chu, X. Gong and J.-A. Duan, Femtosecond laser fabrication of shape-gradient platform: Underwater bubbles continuous self-driven and unidirectional transportation, *Appl. Surf. Sci.*, 2019, **471**, 999–1004.
31 X. Xue, C. Yu, J. Wang and L. Jiang, Superhydrophobic Cones for Continuous Collection and Directional Transportation of CO_2 Microbubbles in CO_2 Supersaturated Solutions, *ACS Nano*, 2016, **10**, 10887–10893.
32 H. Ma, M. Cao, C. Zhang, Z. Bei, K. Li, C. Yu and L. Jiang, Directional and Continuous Transport of Gas Bubbles on Superaerophilic Geometry-Gradient Surfaces in Aqueous Environments, *Adv. Funct. Mater.*, 2017, **28**, 1705091.
33 C. Yu, X. Zhu, K. Li, M. Cao and L. Jiang, Manipulating Bubbles in Aqueous Environment *via* a Lubricant-Infused Slippery Surface, *Adv. Funct. Mater.*, 2017, **27**, 1701605.
34 H. Ye, L. Zhu, W. Li, H. Liu and H. Chen, Constructing Fluorine-Free and Cost-Effective Superhydrophobic Surface with Normal-Alcohol-Modified Hydrophobic SiO2 Nanoparticles, *ACS Appl. Mater. Interfaces*, 2016, **9**, 858–867.
35 W. Liang, L. Zhu, W. Li, X. Yang, C. Xu and H. Liu, Bioinspired Composite Coating with Extreme Underwater Superoleophobicity and Good Stability for Wax Prevention in the Petroleum Industry, *Langmuir*, 2015, **31**, 11058–11066.
36 X. Yang, L. Zhu, Y. Chen, B. Bao, J. Xu and W. Zhou, Controlled hydrophilic/hydrophobic property of silica films by manipulating the hydrolysis and condensation of tetraethoxysilane, *Appl. Surf. Sci.*, 2016, **376**, 1–9.
37 A. Lamoot, A. Uvyn, S. Kasmi and B. G. De Geest, Covalent Cell Surface Conjugation of Nanoparticles by a Combination of Metabolic Labeling and Click Chemistry, *Angew. Chem., Int. Ed.*, 2021, **60**, 6320–6325.
38 X. Chen, R. Chu, T. Xing and G. Chen, One-step preparation of superhydrophobic cotton fabric based on thiol-ene click chemistry, *Colloids Surf., A*, 2021, **611**, 125803.
39 X. Dai, P. Li, Y. Sui and C. Zhang, Synthesis and performance of flexible epoxy resin with long alkyl side chains *via* click reaction, *J. Polym. Sci.*, 2021, **59**, 627–637.
40 X.-M. Fan, J.-J. Shen, Y.-Y. Xu, J. Gao and Y.-W. Zhang, Metabolic integration of azide functionalized glycan on Escherichia coli cell surface for specific covalent immobilization onto magnetic nanoparticles with click chemistry, *Bioresour. Technol.*, 2021, **324**, 124689.
41 X. Liu, F. Wu, K. Cai, Z. Zhao, Z. Zhang, Y. Chen, Y. Liu, J. Cheng and L. Yin, Cancer cell-targeted cisplatin prodrug delivery *in vivo via* metabolic labeling and bioorthogonal click reaction, *Biomater. Sci.*, 2021, **9**, 1301–1312.
42 M. Yu, M. Liu, L. Zhang, M. Li, Y. Hou, D. Wang and S. Fu, Liquid-repellent and self-repairing lubricant-grafted surfaces constructed by thiol-ene click chemistry using

activated hollow silica as the lubricant reservoir, *J. Colloid Interface Sci.*, 2021, **586**, 279–291.

43 P. Tang and G. Sun, Daylight-activated fumigant detoxifying nanofibrous membrane based on thiol-ene click chemistry, *J. Hazard. Mater.*, 2021, **406**, 124723.

44 I. Šarić, M. Kolympadi Markovic, R. Peter, P. Linić, K. Wittine, I. Kavre Piltaver, I. Jelovica Badovinac, D. Marković, M. Knez and G. Ambrožić, In-situ multi-step pulsed vapor phase surface functionalization of zirconia nanoparticles *via* copper-free click chemistry, *Appl. Surf. Sci.*, 2021, **539**, 148254.

45 L. Xiong, W. Guo, B. M. Alameda, R. K. Sloan, W. D. Walker and D. L. Patton, Rational Design of Superhydrophilic/Superoleophobic Surfaces for Oil–Water Separation *via* Thiol–Acrylate Photopolymerization, *ACS Omega*, 2018, **3**, 10278–10285.

46 Q. Wang, Q. Meng, M. Chen, H. Liu and L. Jiang, Bio-Inspired Multistructured Conical Copper Wires for Highly Efficient Liquid Manipulation, *ACS Nano*, 2014, **8**, 8757–8764.

47 J. Ju, K. Xiao, X. Yao, H. Bai and L. Jiang, Bioinspired Conical Copper Wire with Gradient Wettability for Continuous and Efficient Fog Collection, *Adv. Mater.*, 2013, **25**, 5937–5942.

48 K. Li, J. Ju, Z. Xue, J. Ma, L. Feng, S. Gao and L. Jiang, Structured cone arrays for continuous and effective collection of micron-sized oil droplets from water, *Nat. Commun.*, 2013, **4**, 2276.

49 Y. Zheng, H. Bai, Z. Huang, X. Tian, F.-Q. Nie, Y. Zhao, J. Zhai and L. Jiang, Directional water collection on wetted spider silk, *Nature*, 2010, **463**, 640–643.

50 M. Cao, J. Ju, K. Li, S. Dou, K. Liu and L. Jiang, Facile and Large-Scale Fabrication of a Cactus-Inspired Continuous Fog Collector, *Adv. Funct. Mater.*, 2014, **24**, 3235–3240.

51 C. Yu, M. Cao, Z. Dong, J. Wang, K. Li and L. Jiang, Spontaneous and Directional Transportation of Gas Bubbles on Superhydrophobic Cones, *Adv. Funct. Mater.*, 2016, **26**, 3236–3243.

52 L. Lorenceau and D. Qur, Drops on a conical wire, *J. Fluid Mech.*, 2004, **510**, 29–45.

53 J. Masliyah, R. Jauhari and M. Gray, Drag coefficients for air bubbles rising along an inclined surface, *Chem. Eng. Sci.*, 1994, **49**, 1905–1911.

54 J. C. Loudet, P. Hanusse and P. Poulin, Stokes Drag on a Sphere in a Nematic Liquid Crystal, *Science*, 2004, **306**, 1525.

55 C. Zhang, B. Zhang, H. Ma, Z. Li, X. Xiao, Y. Zhang, X. Cui, C. Yu, M. Cao and L. Jiang, Bioinspired Pressure-Tolerant Asymmetric Slippery Surface for Continuous Self-Transport of Gas Bubbles in Aqueous Environment, *ACS Nano*, 2018, **12**, 2048–2055.

56 T. Tate, XXX. On the magnitude of a drop of liquid formed under different circumstances, *London, Edinburgh Dublin Philos. Mag. J. Sci.*, 2009, **27**, 176–180.

57 S. F. Jones, G. M. Evans and K. P. Galvin, Bubble nucleation from gas cavities — a review, *Adv. Colloid Interface Sci.*, 1999, **80**, 27–50.

58 W. Ma, Y. Ding, Y. Li, S. Gao, Z. Jiang, J. Cui, C. Huang and G. Fu, Durable, self-healing superhydrophobic nanofibrous membrane with self-cleaning ability for highly-efficient oily wastewater purification, *J. Membr. Sci.*, 2021, **634**, 119402.

59 W. Liang, L. Zhu, W. Li, C. Xu and H. Liu, Facile Fabrication of Binary Nanoscale Interface for No-Loss Microdroplet Transportation, *Langmuir*, 2016, **32**, 5519–5525.

60 C. Long, Y. Qing, K. An, X. Long, C. Liu, S. Shang, C. Yang and C. Liu, Functional fluorination agents for opposite extreme wettability coatings with robustness, water splash inhibition, and controllable oil transport, *Chem. Eng. J.*, 2021, **415**, 128895.